Optimizing the Performance of CsPbI$_3$-Based Perovskite Solar Cells via Doping a ZnO Electron Transport Layer Coupled with Interface Engineering

Man Yue[1], Jie Su[1] ✉, Peng Zhao[1], Zhenhua Lin[1], Jincheng Zhang[1], Jingjing Chang[1] ✉, Yue Hao[1]

Man Yue and Jie Su have contributed equally to this work.

✉ Jie Su, sujie@xidian.edu.cn; Jingjing Chang, jjingchang@xidian.edu.cn

[1] State Key Discipline Laboratory of Wide Band Gap Semiconductor Technology, Shaanxi Joint Key Laboratory of Graphene, School of Microelectronics, Xidian University, 2 South Taibai Road, Xi'an 710071, People's Republic of China

HIGHLIGHTS

- Device simulations and first-principle calculations are employed to derive a guideline for the optimization of CsPbI$_3$-based perovskite solar cells (PSCs).

- The open voltage and power conversion efficiency of the PSCs are, respectively, improved to 1.31 V and 21.06% by simultaneously introducing an ultra-thin TiO$_2$ buffer layer and increasing the doping concentration of the ZnO electron transport layer.

- The influence of the interfacial buffer layer and doping of the CsPbI$_3$/ZnO interface on PSC performance is discussed.

ABSTRACT Interface engineering has been regarded as an effective and noninvasive means to optimize the performance of perovskite solar cells (PSCs). Here, doping engineering of a ZnO electron transport layer (ETL) and CsPbI$_3$/ZnO interface engineering via introduction of an interfacial layer are employed to improve the performances of CsPbI$_3$-based PSCs. The results show that when introducing a TiO$_2$ buffer layer while increasing the ZnO layer doping concentration, the open-circuit voltage, power conversion efficiency, and fill factor of the CsPbI$_3$-based PSCs can be improved to 1.31 V, 21.06%, and 74.07%, respectively, which are superior to those of PSCs only modified by the TiO$_2$ buffer layer or high-concentration doping of ZnO layer. On the one hand, the buffer layer relieves the band bending and structural disorder of CsPbI$_3$. On the other hand, the increased doping concentration of the ZnO layer improves the conductivity of the TiO$_2$/ZnO bilayer ETL because of the strong interaction between the TiO$_2$ and ZnO layers. However, such phenomena are not observed for those of a PCBM/ZnO bilayer ETL because of the weak interlayer interaction of the PCBM/ZnO interface. These results provide a comprehensive understanding of the CsPbI$_3$/ZnO interface and suggest a guideline to design high-performance PSCs.
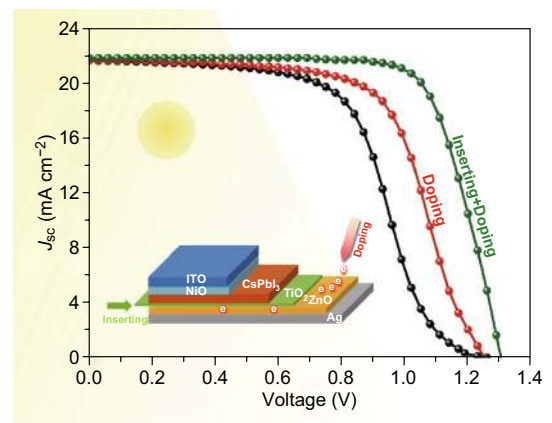
1 Introduction

Organolead halide perovskites (OHPs) have been regarded as promising absorber materials for photovoltaic devices owing to their excellent physical and fabrication properties, such as high absorption coefficients, long charge carrier diffusion lengths, and roll-to-roll processing approaches [1–7]. The record power conversion efficiency (PCE) of OHP solar cells (PSCs) has also increased from 3.8 to 25.2% within the last few years [8]. However, the application of such solar cells is limited by the stability of organic cations given their hygroscopic and volatile nature [9, 10]. To overcome these issues, several theoretical and experimental investigations have been completed to fabricate all-inorganic $CsPbX_3$ perovskites given the instability of PSC with organic cations [11–16]. Moreover, $CsPbX_3$ can sustain temperatures exceeding 400 °C without any phase degradation [17, 18]. $CsPbBr_3$, $CsPbI_3$, $CsPbI_2Br$, and $CsPbIBr_2$ are the most studied all-inorganic perovskites for photovoltaic application [19–22]. Notably, $CsPbBr_3$, $CsPbI_2Br$, and $CsPbIBr_2$ possess large bandgaps that are not ideal or appropriate for a solar cell [23, 24], while $CsPbI_3$ shows a more suitable bandgap of 1.73 eV for photovoltaic application, particularly for a double-junction perovskite/Si tandem [4, 23, 25–27]. Moreover, the PCE of $CsPbI_3$-based PSCs has shown a reproducible photovoltaic performance with a champion efficiency up to 17% [28]. Nevertheless, such reported performances of $CsPbI_3$-based PSCs remain lower than expected.

As is known, the performance of PSCs is not only influenced by the perovskite itself but also strongly affected by the interface between the perovskite and electron transport layer (ETL) which directly affects the collection efficiency of photo-induced charge carriers and PSC stability. To obtain excellent performances of PSCs, several ETLs such as those of titanium oxide (TiO_2), zinc oxide (ZnO), tin dioxide (SnO_2), and n-type organic molecules have been attempted [29–34]. Among them, ZnO has been widely investigated because of its direct wide bandgap, ultra-high electron mobility, transparent properties, and ease of processing at low temperature [30, 35, 36]. Moreover, the ZnO ETL has promoted the open-circuit voltage (V_{oc}) and PCE of $CH_3NH_3PbI_3$-based PSCs to an exciting level ($V_{oc} > 1.20$ V and PCE > 21%) [36, 37]. Nevertheless,

regarding the all-inorganic perovskite-based PSCs with a ZnO ETL, most of their superior performances have yet to be fully realized and few have been studied in practical applications. For example, $CsPbI_2Br$-based PSCs with a ZnO ETL show a low PCE of approximately 13% accompanying a low extraction efficiency and a severe charge recombination [38, 39]. Previous reports regarding OHP-based PSCs have showed that inserting a buffer layer between the perovskite and ETL is an effective means to optimize the performances of OHP-based PSCs [36, 40]. Inspired by these, Jeong et al. [41] inserted poly(ethylene oxide) between the $CsPbI_3$ and ZnO ETL to enhance the phase stabilization of α-$CsPbI_3$. Our previous studies have employed an MoO_3 interfacial layer to enhance charge extraction and suppress carrier recombination of a $CsPbI_2Br$-based PSC [13]. Nevertheless, the performances of $CsPbI_3$-based PSCs remain lower than expected. The influential mechanisms of these methods on all-inorganic $CsPbI_3$ devices have not yet been comprehensively investigated. To further understand the effects of inserting a layer, the $CsPbI_3$-based PSCs with a ZnO ETL coupling with ultra-thin PCBM and TiO_2 inserting layers are designed and investigated by device simulations and first-principle calculations. In addition, previous studies have showed that doping the ETL is another means to tune the performances of PSCs. Metal ion (e.g., Mg, Li, Al, and Nb)-doped ZnO has been used as an efficient ETL to enhance the PCE to greater than 19% [42–44]. Moreover, novel molecular (e.g., triphenylphosphine oxide (TPPO) and phenyl-C61-butyric acid methyl ester (PCBM)) doping of the ETL has relieved the current hysteresis and increased the PCE of an OHP-based PSC from 19.01 to 20.69%. Inspired by these results, modulating the doping concentration in the ZnO layer of a $CsPbI_3$-based PSC with PCBM and TiO_2 inserting layers is employed to further improve the performances of $CsPbI_3$-based PSCs in this study.

Herein, the device simulations implemented in the Silvaco technology computer-aided design (TCAD) simulation code and the first-principle calculations implemented in the Vienna Ab initio simulation package (VASP) codes are employed to investigate the $CsPbI_3$/ZnO interface of $CsPbI_3$-based PSCs. The energy bands, photo-generation rate, current density–voltage (J–V) characteristics, and spectral response can be calculated by Silvaco TCAD. The interfacial properties based on

electronic and atomic structures can be showed by the first-principle calculations. Consequently, the optimal doping concentration of ZnO ETL and the thicknesses of the TiO_2 and PCBM insertion layers are obtained. At the same time, the effects and mechanisms of the doping concentration and insertion layers on the PCE, V_{oc}, fill factor (FF), and current tailing phenomenon are analyzed by energy bands, photo-generation rate, interfacial structures, and density of states (DOSs). Moreover, the 1-nm ultra-thin TiO_2 insertion layer coupling with the doped ZnO layer at a 10^{22} cm^{-3} doping concentration can improve the V_{oc} and PCE of the $CsPbI_3$-based PSCs from 1.25 V and 15.09% to 1.31 V and 21.06%, respectively. Our work can provide important guidance and understanding for device design and optimization from the considerations of theory.

2 Simulation Methods

All device simulations were conducted using Silvaco TCAD which was mainly based on the Poisson equation (Eq. 1), carrier continuity equation (Eq. 2), and drift–diffusion equation (Eq. 3) as follows [4, 31]:

$$\frac{a^2\varphi}{ax^2} = \frac{q}{\varepsilon}(n - p) \tag{1}$$

$$\frac{an}{at} = \frac{1}{q}\frac{aJ_n}{ax} + G - R \frac{ap}{at} = -\frac{1}{q}\frac{aJ_p}{ax} + G - R \tag{2}$$

$$J_n = qD_n\frac{a_n}{ax} - q\mu_n\frac{a_\varphi}{ax} J_p = -qD_p\frac{a_p}{ax} - q\mu_p\frac{a_\varphi}{ax} \tag{3}$$

where J_n is the electron current density, J_p is the hole current density, D_n is the electron diffusion coefficient, D_p is the hole diffusion coefficient, μ_n is the electron mobility, μ_p is the hole mobility, φ is the electric potential, ε is the dielectric constant, q is the electron charge, n is the electron concentration, p is the hole concentration, G is the carrier generation rate, and R is carrier recombination rate. In the simulation, Shockley–Read–Hall (SRH), band-to-band, and Auger recombinations were considered. The transfer-matrix method (TMM) was used as an optical model to calculate the carrier generation rate $G(x)$ [45]. According to Eqs. (4) and (5), the optical electric field $|E(x)|^2$ should be obtained before calculating the carrier generation rate. Here, ε_0, c, k, n, h, and λ are the vacuum permittivity, light speed, imaginary part of the refractive index, real part of the refractive index, Planck constant, and wavelength, respectively:

$$Q(x, \lambda) = \frac{2\pi c\varepsilon_0 kn|E(x)|^2}{\lambda} \tag{4}$$

$$G(x) = \int_{\lambda_1}^{\lambda_2} \frac{\lambda}{hc}Q(x, \lambda)d\lambda. \tag{5}$$

In addition, the standard AM 1.5 G solar spectrum was used to measure the J–V curve under illumination. Such approaches have been widely employed to investigate the optical behaviors of photovoltaics based on perovskites [4, 5, 31, 46–48].

The inverted PSCs based on $CsPbI_3$ in this study are shown in Fig. 1. $CsPbI_3$ was employed as an absorber layer and NiO as a hole transport layer. The electron transport layers included a ZnO single layer, TiO_2/ZnO, and PCBM/ZnO bilayer, respectively. During the experiment, the similar structure device Au/NiO/CsPbBr3/ZnO/ITO/glass was successfully prepared [34]. To comprehensively understand the mechanism of the ETL and eliminate the effect of the hole transport layer, the optimal thickness of the NiO hole transport layer was set to 30 nm and was unchanged after an extensive test as shown in Fig. S1.

All first-principle density functional theory calculations were performed using the projector augmented wave method (PAW) and Perdew–Burke–Ernzerhof (PBE) implemented in the VASP code [49–51]. The convergence criterions were 1×10^{-5} eV for the self-consistent field energy and 0.01 eV Å^{-1} for the residual forces on each atom, respectively. A cutoff energy of 400 eV and a k-point sampling at the gamma point were employed.
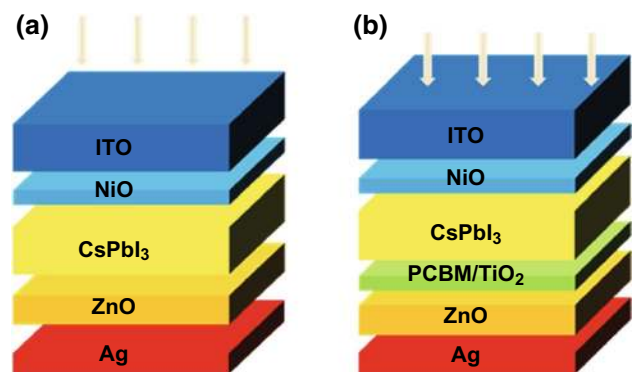
Fig. 1 Schematic device structure of the $CsPbI_3$-based PSCs with **a** ZnO single-layer and **b** TiO_2 (PCBM)/ZnO bilayer ETL

The CsPbI$_3$/ZnO interface models were constructed using a 1×1 supercell of the CsPbI$_3$ (001) surface and a 2×2 supercell of the ZnO (001) surface. A vacuum of 15 Å was considered along the z direction to avoid artificial interlayer interactions.

3 Results and Discussion

According to previous studies, both the thicknesses of the absorber layer and electron transport layer strongly affect the performance of a solar cell device; thus, it is necessary to optimize the thicknesses of the perovskite and ZnO ETL. Figure 2a shows the short-circuit current density (J_{sc}) for the CsPbI$_3$-based PSCs with a single-layer ZnO ETL depending on the thickness of the CsPbI$_3$. The electrical parameters of such PSCs are summarized in Table 1 [23, 24, 31, 52, 53]. J_{sc} sharply increases at first and then decreases with

Table 1 Simulation parameters of the perovskite solar cell, where ε_r is the dielectric constant, E_g is the bandgap, λ is the electron affinity, N_c is the effective conduction band density, N_v is the effective valence band density, μ_n is the electron mobility, and μ_p is the hole mobility

Parameters	NiO	CsPbI$_3$	PCBM	ZnO	TiO$_2$
Thickness (nm)	30	200	8	40	1
ε_r	12	6	4	9	100
E_g (eV)	3.6	1.73	2	3.3	3.2
λ (eV)	1.7	3.6	3.9	4.4	4
N_C (cm^{-3})	2.5×10^{20}	1.49×10^{18}	1×10^{21}	2.2×10^{18}	1×10^{21}
N_V (cm^{-3})	2.5×10^{20}	2.2×10^{18}	2×10^{20}	1.8×10^{19}	2×10^{20}
N_A (cm^{-3})	1×10^{16}	–	–	–	–
N_D (cm^{-3})	–	–	1×10^{20}	1×10^{20}	1×10^{20}
μ_n (cm^2 V^{-1} s^{-1})	0.01	25	0.01	100	0.006
μ_p (cm^2 V^{-1} s^{-1})	0.01	25	0.01	25	0.006
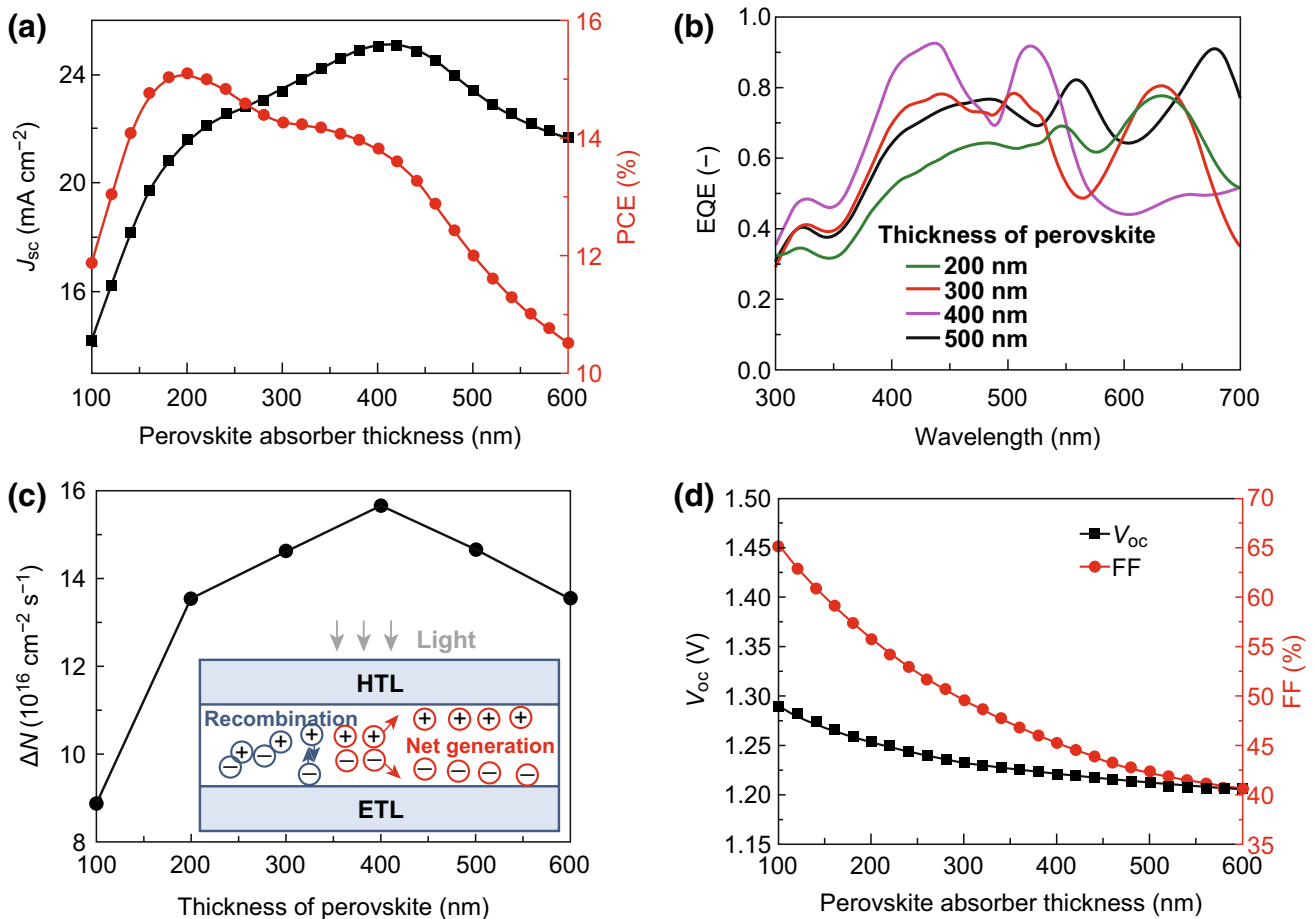
Fig. 2 a, **d** Device parameters as functions of the perovskite thickness for a CsPbI$_3$-based PSC with a single-layer ZnO ETL. **b** EQE spectra and **c** net carrier generation rate for CsPbI$_3$-based PSCs with a single-layer ZnO ETL under different perovskite thickness conditions

increasing perovskite thickness. The maximum J_{sc} reaches 25.05 mA cm^{-2} when the perovskite thickness reaches 420 nm. This can be attributed to the variation in the external quantum efficiency (EQE) and net carrier generation rate (ΔN) of the PSCs as shown in Fig. 2b, c. It can be seen that the EQE of the PSCs is enhanced with the increasing thickness of the CsPbI$_3$, suggesting the stronger photo-absorption and higher carrier generation rate. Meanwhile, the carrier diffusion length of CsPbI$_3$ of approximately 1.5 μm [54] is longer than its thickness. This might result in increasingly more generated carriers being collected by electrodes with negligible recombination. As a consequence, the ΔNs (the carrier generation rate subtracted by the carrier

recombination rate) of the PSCs shifts up accompanying the enhanced J_{sc}, as shown in Fig. 2c. When the CsPbI$_3$ thickness continues to increase and exceeds 420 nm, the EQE of the PSC decreases and this in turn decreases the carrier generation rate. Meanwhile, the enhanced thickness can enlarge the recombination rate of the generated carriers. As a result, the less generated carries are collected by electrodes, leading to the reduced net carrier generation rates of the PSCs accompanying the decreasing J_{sc}. For the PCE of the CsPbI$_3$-based PSCs, its variation is similar to that of J_{sc} except for the thickness corresponding to the maximum PCE, as shown in Fig. 2a. The maximum PCE of the CsPbI$_3$-based PSC with a single-layer ZnO ETL is 15.09%, and the corresponding thickness of the CsPbI$_3$ perovskite is approximately 200 nm rather than 420 nm. Thus, 200-nm CsPbI$_3$ is employed in the following discussion. Notably, such characteristics are different from those of OHP-based PSCs [4, 31, 46, 55] because both the V_{oc} and FF monotonously decrease as the thickness of the CsPbI$_3$ increases from 100 to 600 nm, which is different from that of J_{sc}, as shown in Fig. 2d and previous reports regarding OHP-based PSCs [4, 31]. To elucidate such variation, Fig. 3 shows the quasi-Fermi level with different perovskite layer thicknesses because the difference between the quasi-Fermi levels directly affects the energy required for carrier transition. It is obvious that the difference between the electron quasi-Fermi level (E_{fn}) and hole quasi-Fermi level (E_{fh}) decreases with the increase in the perovskite layer thickness, which corresponds with the continuously decreased energy required for
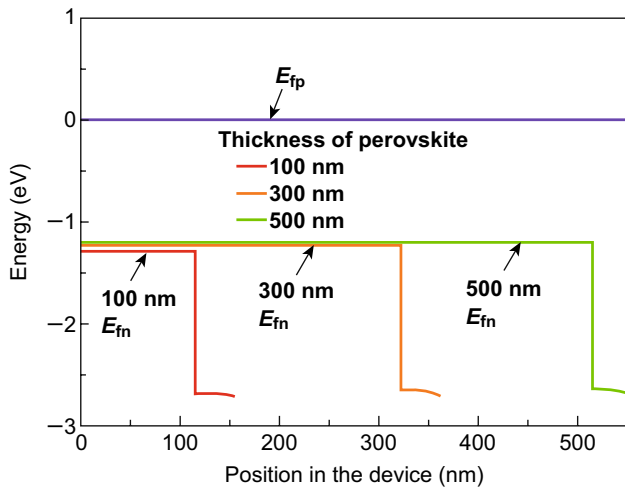

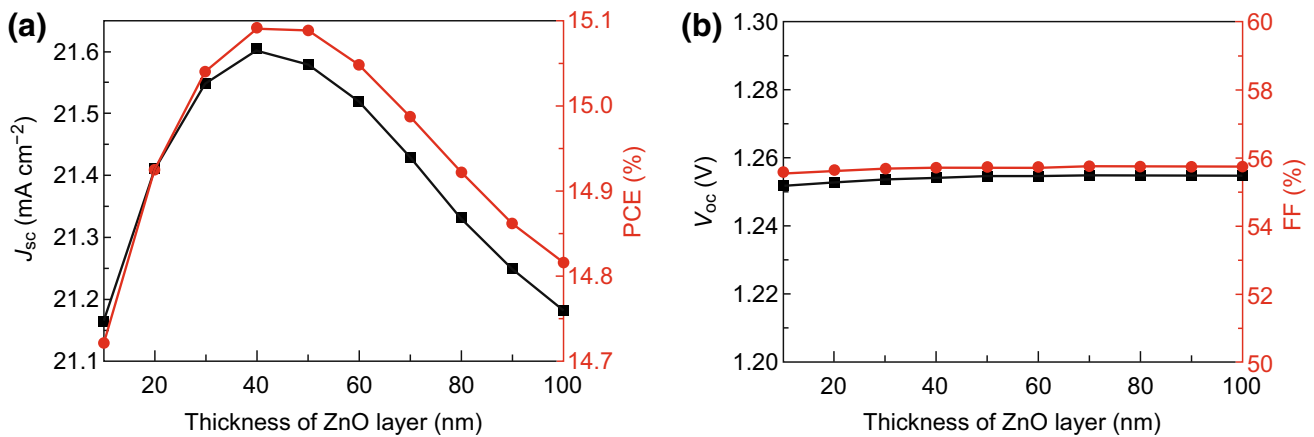**Fig. 3** Quasi-Fermi level with different perovskite layer thicknesses

Fig. 4 Device parameters as a function of the thickness of ZnO for the CsPbI$_3$-based PSC with a single-layer ZnO ETL

carrier transition. Thus, the V_{oc} monotonously decreases as the CsPbI$_3$ thickness increases.

Figure 4 shows the performance of CsPbI$_3$-based PSCs with a single-layer ZnO ETL as a function of the ZnO thickness. Here, the CsPbI$_3$ thickness is set to 200 nm. It was found that the J_{sc} increases as the ZnO layer thickness increases from 10 to 40 nm and then decreases with the continued increasing thickness of the ZnO layer. The EQE of the PSC, which directly determines the numbers of generated carriers, first increases and then decreases with the increasing thickness of the ZnO layer, as shown in Fig. S2a. In other words, as the ZnO layer thickness continues to increase, the net carrier generation rate of the PSC cannot monotonously increase but reaches a peak value immediately when the ZnO layer thickness is 40 nm, as shown in Fig. S2a. As a result, J_{sc} shows its highest value of approximately 21.61 mA cm^{-2} when the ZnO layer thickness is 40 nm. Such similar variation characteristics are also suitable to the change in the PCE with the increasing thickness of the ZnO layer because the V_{oc} and FF remain unchanged irrespective of the thickness of the single-layer ZnO (Fig. 4b). This is because the net carrier generation rate has not influenced the band energy and interfacial structure of the CsPbI$_3$/ZnO interface which are the intrinsic properties of the fabricated PSC. The differences between the band edges of the perovskite and ZnO layers that directly affect the V_{oc} and the defect states density that affects the FF remain unchanged even if the thickness of the ZnO layer increases, as shown in Fig. S2b. Thus, the optimal thickness of the ZnO ETL is 40 nm and the optimized PCE is approximately 15.09%.

In addition, notably, although the V_{oc} is sufficiently large (approximately 1.254 V), the PCE and FF are far lower than those of the OHP-based PSCs [46]. An obvious current trailing in the J–V curve, which is related to the conductivity of ETL, is observed for the CsPbI$_3$-based PSCs with a single-layer ZnO ETL, as shown in Fig. S3. Thus, doping of an ETL, such as an in-doped ZnO ETL, has been employed to improve the performance of the PSCs during experiments [56]. Nevertheless, the optimal doping concentration and doping mechanism have not yet been determined. Figure 5a shows the J_{sc} of a CsPbI$_3$-based PSC with a different doping concentration in the single-layer ZnO ETL. It was found that the J_{sc} shifts up at first as the doping concentration increases and then reaches a maximum value of approximately 21.62 mA cm^{-2} at a doping concentration of approximately 10^{21} cm^{-3} before and finally shifting down as the doping concentration continues to increase. However, the net carrier generation rates first increase and then approach a constant with increasing doping concentration. On the one hand, the dopant can improve the charge density (Fig. S4) and then improve the conductivity of the ZnO layer such that the recombination rate of the photo-generated carrier around the interface decreases. On the other hand, the doping concentration in the single-layer ZnO ETL has a negligible influence on the EQE (Fig. S5) such that the number of photo-generated carriers remains unchanged. As a result, the dopant increases the net carrier generation rate (Fig. 5a) and then improves the short-circuit current density. Note that although the dopant improved the photo-generated carrier density, the dopant inevitably induces impurity scattering, which can deteriorate the carrier mobility. When the doping concentration is sufficiently large, the negative effect of impurity scattering can outweigh the positive effect of the dopant, leading to a stronger reduction in the carrier mobility than the increment of the carrier density. Meanwhile, the highest carrier recombination rate of a semiconductor is closely related to the temperature and independent of the carrier concentration [57]. Consequently, the short-circuit current density decreases, and the net carrier generation rate remains constant when the doping concentration of the ZnO layer is larger than 10^{21} cm^{-3}. In addition, because of the enhanced conductivity via the dopant, less carriers are accumulated in the CsPbI$_3$/ZnO contact region, which relieves the obvious current trailing in the J–V curve, as shown in Fig. 5b. Owing to the reduced current trailing, both the FF and PCE of the CsPbI$_3$-based PSC with a single-layer ZnO ETL monotonically increase with increasing doping concentration (in Fig. 5c). Nevertheless, it is interesting that the V_{oc} remains at a value of 1.254 V as the doping concentration increases and then slightly decreases when the doping concentration in the single-layer ZnO ETL is higher than 10^{20} cm^{-3}. Although both the band edges of the CsPbI$_3$ and ZnO at the CsPbI$_3$/ZnO contact region continually shift down with increasing doping concentration, the difference between the conduction band maximum (CBM) of the CsPbI$_3$ and valence band minimum (VBM) of the ZnO remains constant, leading to an unchanged built-in electric field at the CsPbI$_3$/ZnO contact. Furthermore, when the doping concentration in the single-layer ZnO ETL is greater than 10^{20} cm^{-3}, the reduced CBM of the ZnO ETL is lower than the Fermi level of the electrode, which can induce an opposite electric field at the ZnO/Ag contact and then offset
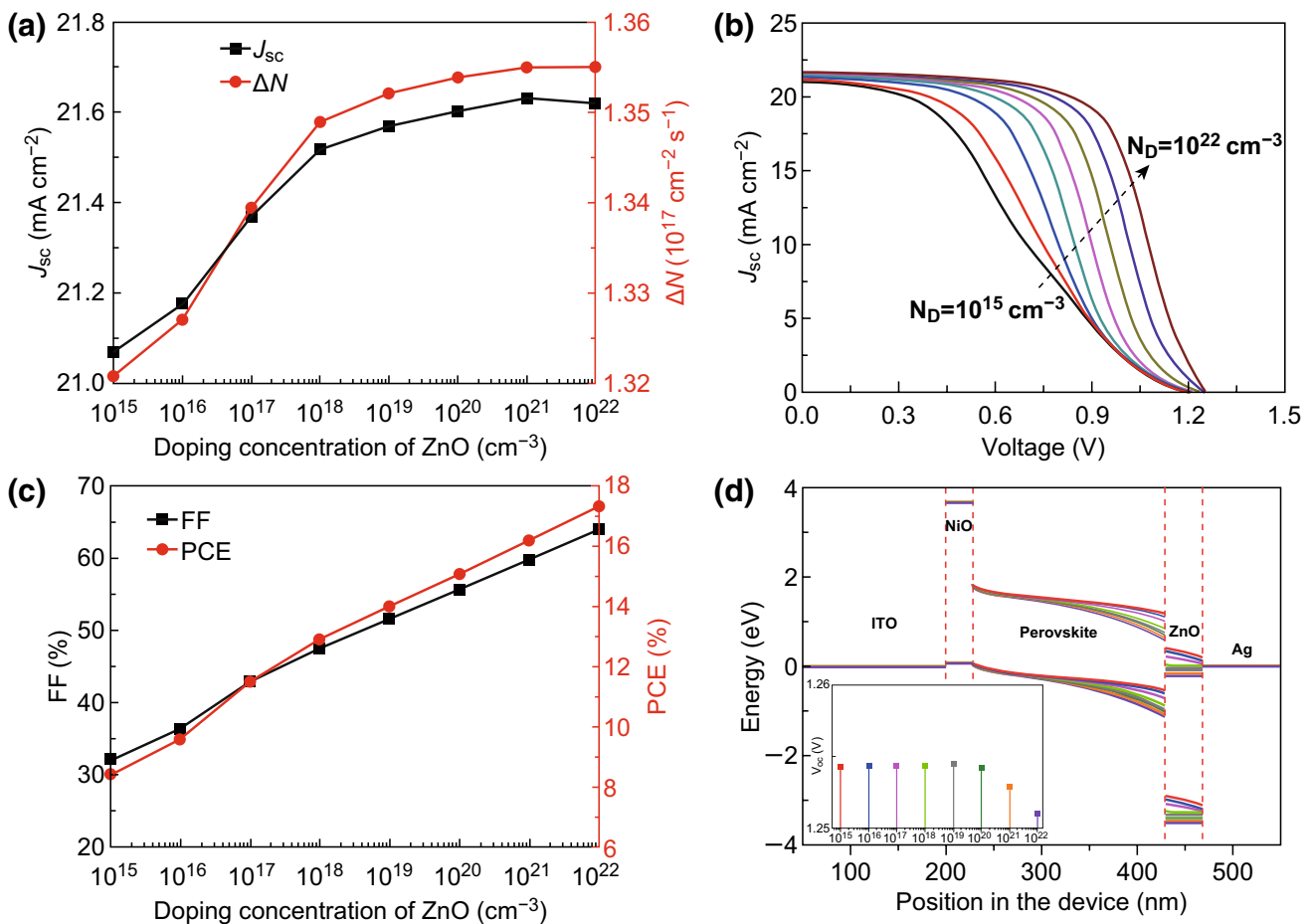
Fig. 5 **a** Short-circuit current density (J_{sc}) and net carrier generation rate (ΔN), **b** J–V curves, **c** fill factor (FF) and power conversion efficiency (PCE), and **d** energy band diagrams coupled with open-circuit voltage V_{oc} of CsPbI$_3$-based PSCs at different doping concentrations

the partial electric field at the CsPbI$_3$/ZnO contact. Thus, the V_{oc} slightly decreases when the doping concentration in the single-layer ZnO ETL is greater than 10^{20} cm^{-3}, as shown in the inset of Fig. 5d.

Except for doping of the ETL, inserting an additional ultra-thin buffer layer between the perovskite and ETL to form a bilayer ETL has also been employed to improve the performance of PSCs [58]. Here, PCBM and TiO$_2$ are selected as the additional buffer layers and combined with the ZnO electron transport layer to form PCBM/ZnO and TiO$_2$/ZnO bilayer ETLs (as shown in Fig. 1). Meanwhile, the ZnO doping concentration is set to 10^{20} cm^{-3}. To exclude the effect of CsPbI$_3$ thickness, the thicknesses of all CsPbI$_3$ parts are set to 200 nm. For the CsPbI$_3$-based PSC with a PCBM/ZnO bilayer ETL, its device parameters (J_{sc}, V_{oc}, FF, and PCE) are dependent on the thickness of PCBM layer as

shown in Fig. 6. Both the J_{sc} and PCE increase first and then decrease with the increasing thickness of the PCBM part. Meanwhile, the V_{oc} and FF first shift down and up, respectively, and then approach constants as the PCBM thickness increases. Moreover, all the device parameters achieve their highest values when the PCBM thickness is 8 nm. Thus, the optimal thickness of PCBM for the CsPbI$_3$-based PSC with a PCBM/ZnO bilayer ETL is 8 nm. For the CsPbI$_3$-based PSC with a TiO$_2$/ZnO bilayer ETL, all device parameters, except for FF, decrease with increasing thickness of the TiO$_2$ part. Meanwhile, the FF first decreases and then slightly increases with the increasing thickness of the TiO$_2$ part. During the experiment, the insertion layers between the perovskite and ETL are typically ultra-thin. Hence, the optimal thickness of the TiO$_2$ layer for the CsPbI$_3$-based PSC with a TiO$_2$/ZnO bilayer ETL may be 1 nm.
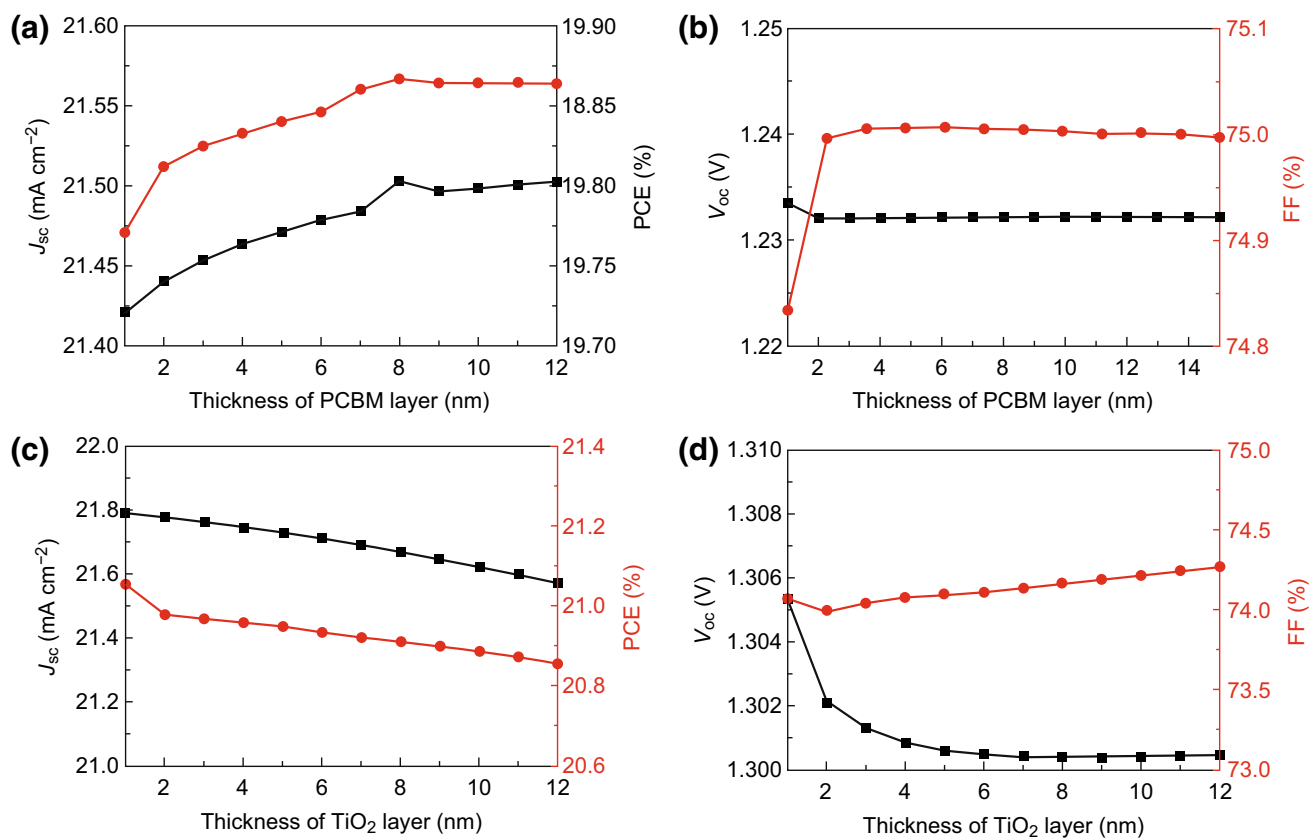
Fig. 6 Device parameters as functions of **a**, **b** the thickness of the PCBM layer for a PSC with a PCBM/ZnO bilayer ETL and **c**, **d** the thickness of the TiO_2 layer for a PSC with TiO_2/ZnO bilayer ETL
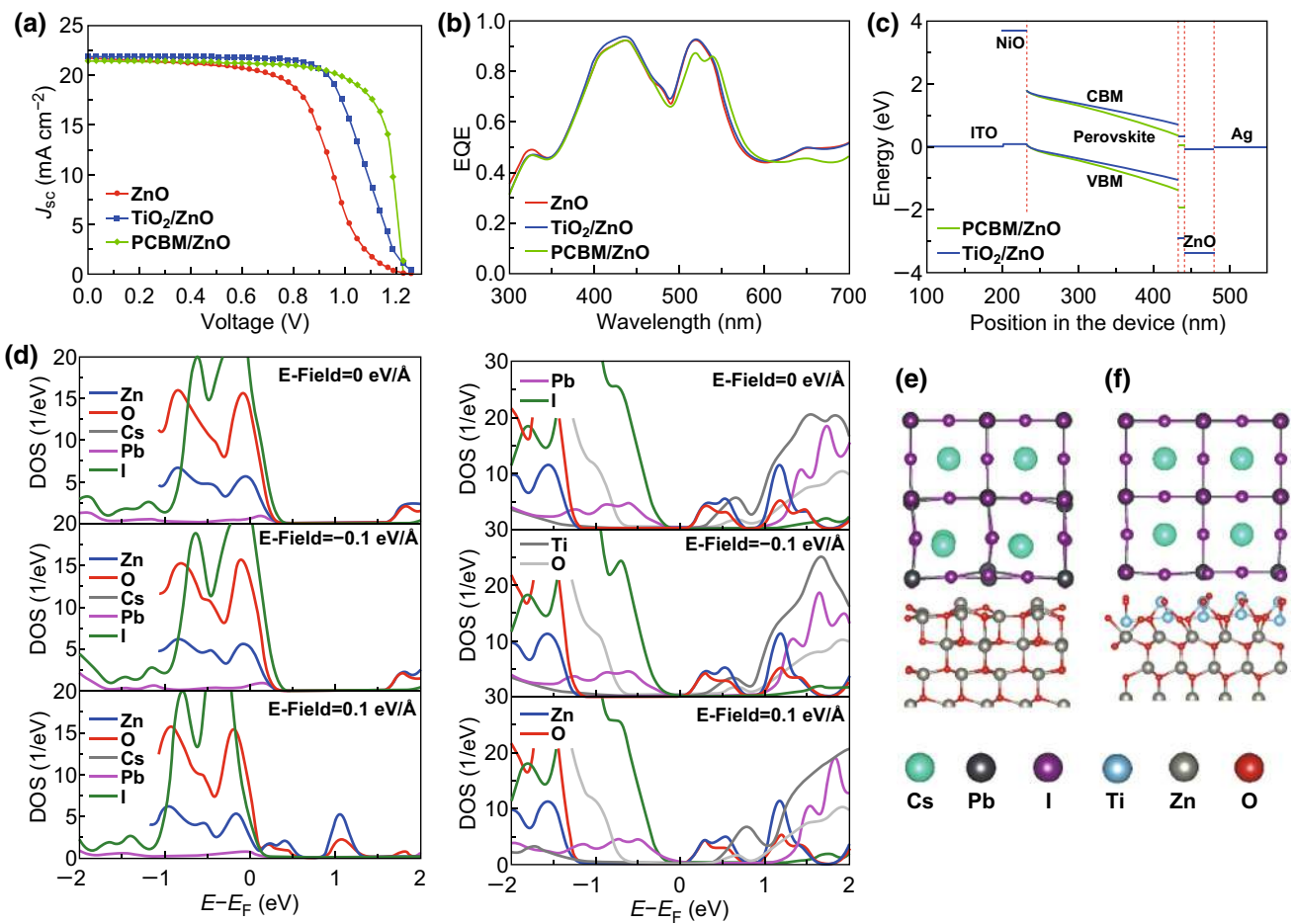
Table 2 Parameters of $CsPbI_3$-based PSCs with a ZnO single-layer ETL, PCBM/ZnO bilayer ETL, and TiO_2/ZnO bilayer ETL

Structure	Doping concentration (cm^{-3})	ΔN (cm^{-2} s^{-1})	J_{sc} (mA cm^{-2})	V_{oc} (V)	FF (%)	PCE (%)
ZnO	10^{20}	1.35×10^{17}	21.60	1.25	55.75	15.09
PCBM/ZnO		1.34×10^{17}	21.50	1.23	74.99	19.87
TiO_2/ZnO		1.36×10^{17}	21.83	1.31	65.34	18.64
ZnO	10^{22}	1.35×10^{17}	21.55	1.25	64.12	17.34
PCBM/ZnO		1.34×10^{17}	21.48	1.23	75.00	19.87
TiO_2/ZnO		1.36×10^{17}	21.79	1.31	74.07	21.06

Table 2 lists the PCEs of the $CsPbI_3$-based PSCs with a ZnO single-layer ETL, PCBM/ZnO bilayer ETL, and TiO_2/ZnO bilayer ETL. The detailed calculation parameters are listed in Table S1. Evidently, the PCEs of the $CsPbI_3$-based PSCs with a single-layer ZnO ETL can be enlarged by using a bilayer ETL substituting for the single-layer ETL. Under a doping concentration of approximately 10^{20} cm^{-3}, the highest PCEs of the $CsPbI_3$-based PSCs with a PCBM/ ZnO bilayer ETL and TiO_2/ZnO bilayer ETL are 19.87% and 18.64%, respectively, which are greater than that of the $CsPbI_3$-based PSC with a single-layer ZnO ETL (approximately 15.09%). Although these values deviate from the corresponding experimental values, such variation characteristics are consistent with the experimental results [36, 37]. Because the structural variation of the ETL shows a slight effect on the EQE, it further weakens the current trailing

Fig. 7 **a** *J–V* characteristics of PSCs with a ZnO single-layer ETL, PCBM/ZnO bilayer ETL, and TiO$_2$/ZnO bilayer ETL under a simulated AM 1.5 G illumination of 100 mW cm^{-2}, in which the doping concentration of the ZnO layer is 10^{20} cm^{-3}. **b** EQE spectra of devices based on a 200-nm perovskite layer with different ETLs. **c** Energy band diagrams of the device with a PCBM/ZnO bilayer. **d** DOS of the CsPbI$_3$/ZnO and CsPbI$_3$/TiO$_2$/ZnO interfaces under different electronic fields. The optimized structures of **e** CsPbI$_3$/ZnO and **f** CsPbI$_3$/TiO$_2$/ZnO interfaces are shown

in the *J–V* curve and then enhances the FF, as shown in Fig. 7a, b and Table 2. However, the increment of the FF of the CsPbI$_3$-based PSC with a TiO$_2$/ZnO bilayer ETL is inconspicuous such that the PCE of the CsPbI$_3$-based PSC with a TiO$_2$/ZnO bilayer ETL is lower than that with a PCBM/ZnO bilayer ETL. Notably, the current trailing is not only related to the conductivity of the ETL but also the ion migration and phase separation. Taking the PSC with a TiO$_2$/ZnO bilayer ETL as an example, the orbital contributions to the CBM (Zn-*d* and O-*p* orbitals) and VBM (Pb-*p* and I-*p* orbitals) of the CsPbI$_3$/TiO$_2$/ZnO interfaces are unchanged by small external negative (− 0.1 eV Å^{-1}) and positive (0.1 eV Å^{-1}) electric fields. Meanwhile, the bandgap is slightly changed by the small external electric

field. Such characteristics are different from those of the CsPbI$_3$/ZnO interfaces, as shown in Fig. 7d, which suggests weaker ion migration for the CsPbI$_3$/TiO$_2$/ZnO interface compared to that of the CsPbI$_3$/ZnO interface [59]. However, the disordered octahedron of CsPbI$_3$ at the CsPbI$_3$/ZnO interface region is significantly ordered upon forming the CsPbI$_3$/TiO$_2$/ZnO interface, relieving the phase separation and interfacial gap states induced by the disordered octahedron of CsPbI$_3$ (Fig. 7e, f). In addition, notably, V_{oc} is tuned during the process of improved current trailing in the *J–V* curve (Fig. 7a). The V_{oc} can be decreased and increased to 1.23 and 1.31 V by the TiO$_2$/ZnO and PCBM/ZnO bilayer ETL, respectively, as listed in Table 2. The main reason for this is that the additional PCBM film slightly enhances the

band bending of the $CsPbI_3$ surface at the perovskite/ZnO interface region and then weakens the built-in electric field (viz. the difference between the CBM of $CsPbI_3$ and VBM of ZnO as shown in Fig. 7c), while the additional TiO_2 introduces an opposite effect. From Fig. 7, it can be observed that the TiO_2/ZnO bilayer ETL slightly improves the J_{sc} of the $CsPbI_3$-based PSC to 21.83 mA cm^{-2}, although it shows a negligible influence on the EQE of the $CsPbI_3$-based PSC because the fewer interfacial gap states induced by the TiO_2/ZnO bilayer ETL can reduce the carrier recombination. In contrast, the PCBM/ZnO bilayer ETL slightly reduces the J_{sc} of the $CsPbI_3$-based PSC to 21.50 mA cm^{-2} because the corresponding bilayer ETL slightly weakens the EQE and the net carrier generation rate ΔN, as shown in Fig. 7b and Table 2.

Notably, although the PCE was significantly improved by employing the bilayer ETL, the FF of the $CsPbI_3$-based PSCs with a TiO_2/ZnO bilayer and the V_{oc} of the $CsPbI_3$-based PSCs with a PCBM/ZnO bilayer remained lower than expected values. It can be speculated that the PCE can be further improved if the FF and V_{oc} are increased. The aforementioned analysis shows that increasing the doping concentration in the ZnO ETL can not only relieve the current trailing in the J–V curve but also tune the energy of the band level. According to such a mechanism, it can be speculated that the performance of the $CsPbI_3$-based PSC with a bilayer ETL can be further improved by increasing the doping concentration of the ZnO layer. The J–V curves of the $CsPbI_3$-based PSCs with a bilayer ETL when the doping concentration of the ZnO layer increases to 10^{22} cm^{-3} are

shown in Fig. 8a. Table 2 lists the device parameters of the PSCs with bilayer ETLs and a high doping concentration (approximately 10^{22} cm^{-3}). For the PSC with a TiO_2/ZnO bilayer ETL, its PCE is strongly increased to 21.06% by the increased doping concentration in the ZnO layer because of the enlarged FF of approximately 74.07%. These values are far higher than not only those of the PSC with a TiO_2/ZnO bilayer ETL and low doping concentration and the PSC with a single-layer ZnO ETL and high doping concentration but also those of previous reports [16, 28, 60–65] as listed in Table 2 and shown in Fig. 8b. As shown in Fig. S6, there is a high charge density at the TiO_2/ZnO contact, suggesting strong interaction and low contact resistance between the TiO_2 and ZnO layers. Upon increasing the doping concentration in the ZnO layer, the charge density at the TiO_2/ZnO contact can be further improved which is beneficial in decreasing the contact resistance between the TiO_2 and ZnO layers. Meanwhile, because of the strong interlayer interaction at the TiO_2/ZnO contact, the increment of the doping concentration promotes more carrier transfer to the TiO_2 buffer layer and improves the conductivity of the TiO_2/ZnO bilayer ETL. As a result, the FF of the PSC with a TiO_2/ZnO bilayer ETL increased as the doping concentration in the ZnO layer increased. However, notably, the increased doping concentration in the ZnO layer does not affect the V_{oc} and slightly reduces the J_{sc} of the PSC with a TiO_2/ZnO bilayer ETL. Because the band levels of the $CsPbI_3$ perovskite and the work function of the electrodes remain unchanged, the increased doping concentration shifts the band levels of the ZnO layer downward, as shown in Fig. S7. In other words,
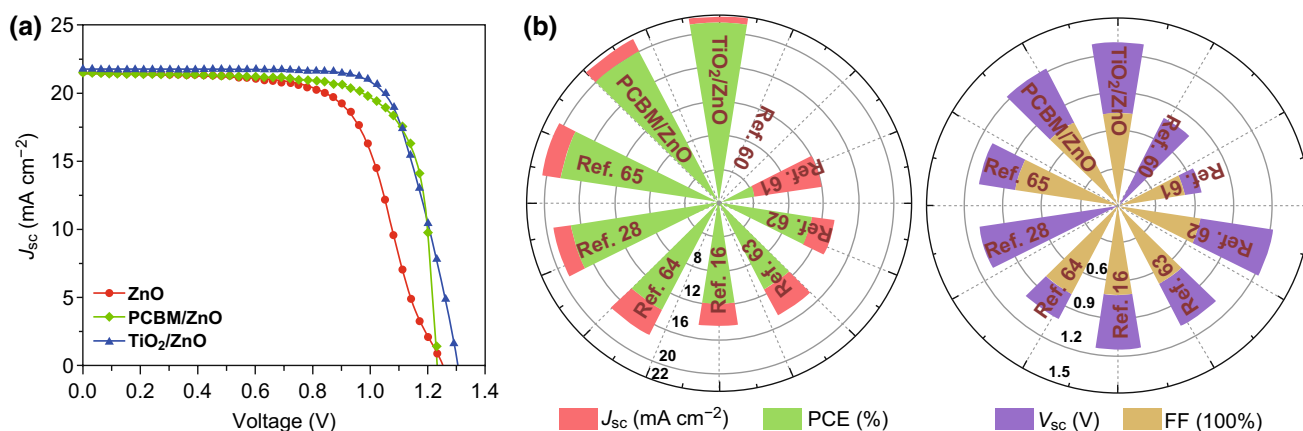
Fig. 8 **a** J–V characteristics of PSCs with a ZnO single-layer ETL, PCBM/ZnO bilayer ETL, and TiO_2/ZnO bilayer ETL at a doping concentration for the ZnO layer of 10^{22} cm^{-3}. **b** Device parameters of PSCs with PCBM/ZnO bilayer ETLs and TiO_2/ZnO bilayer ETLs optimized by a doping concentration of approximately 10^{22} cm^{-3} in the ZnO layer coupled with the reported device performances of the $CsPbI_3$-based PSCs

the increment of the positive built-in electric field between the perovskite and ETL equals the increment of the negative built-in electric field between the ETL and electrodes, such that the built-in electric field of the PSC remains unchanged and does not affect the V_{oc}. In addition, the enlarged doping concentration of the ZnO in the bilayer ETL has a negligible effect on the EQE and net carrier generation rate (Table 2 and Fig. S8), but it can deteriorate the carrier mobility, such that the J_{sc} of the PSC with a TiO$_2$/ZnO bilayer ETL slightly decreases. These mechanisms are also suitable to the PSC with a PCBM/ZnO bilayer ETL as shown in Figs. S6–S8. Hence, upon increasing the doping concentration of the ZnO layer in the PSC with a PCBM/ZnO bilayer ETL, its variations in J_{sc} and V_{oc} are same as those of a PSC with a TiO$_2$/ZnO bilayer ETL, as listed in Table 2. However, notably, the interlayer interaction between the PCBM and ZnO layer is weak and close to van der Waals interaction, because of low charge density between the PCBM and ZnO layers shown in Fig. S6. Therefore, increasing the doping concentration of the ZnO layer has difficulty improving the charge density between the PCBM and ZnO layers and then enhances the conductivity of the PCBM/ZnO bilayer ETL. Hence, the increased doping concentration does not affect the FF and PCE of the PSC with a PCBM/ZnO bilayer ETL. Moreover, although the improved performances of the PSC with a PCBM/ZnO bilayer ETL are superior to those of other CsPbI$_3$-based PSCs [16, 28, 60–65], they are lower than those of the PSC with a TiO$_2$/ZnO bilayer ETL, as shown in Fig. 8b. According to the aforementioned analysis, it can be found that modulating the doping concentration of the ZnO layer in the bilayer ETL is an effective means to improve the performance of the PSC with a bilayer ETL when the buffer layer strongly interacts with the ZnO ETL.

4 Conclusions

Using device simulations coupled with first-principle calculations, doping engineering of the ZnO ETL and CsPbI$_3$/ZnO interface engineering by inserting additional PCBM and TiO$_2$ buffer layers are employed to improve the performances of the CsPbI$_3$-based PSCs. The results demonstrate that increasing the doping concentration of the ZnO layer alone can relieve the current trailing and introduce the opposite built-in electric field at the ZnO/electrode contact, increasing the FF and decreasing the V_{oc}. Meanwhile,

separately inserting a TiO$_2$ buffer layer can reduce the band bending and disordered structure of CsPbI$_3$, increasing the V_{oc} and PCE. Interestingly, combining these two methods can improve the V_{oc}, FF, and PCE of the CsPbI$_3$-based PSC to 1.31 V, 74.07%, and 21.06%, respectively, because the doping concentration of the ZnO layer in the TiO$_2$/ZnO bilayer ETL does not affect the band bending but strongly tunes the conductivity of the TiO$_2$/ZnO bilayer ETL. However, the performances of the CsPbI$_3$-based PSC with a PCBM/ZnO bilayer ETL are irrespective of the doping concentration in the ZnO layer because the weak interlayer interaction between the PCBM and ZnO layers impedes the effect of the doping concentration in the ZnO layer on the PCBM layer. In addition, these variations are elucidated by the band alignment, density of states, and octahedron order of the corresponding CsPbI$_3$/ZnO interfaces. These results provide a comprehensive understanding of the CsPbI$_3$/ZnO interface and suggest a guideline to design a high-performance PSC.

References

1. Z. Liu, J. Chang, Z. Lin, L. Zhou, Z. Yang et al., High-performance planar perovskite solar cells using low temperature, solution–combustion-based nickel oxide hole transporting layer with efficiency exceeding 20%. Adv. Energy Mater. **8**, 1703432 (2018). https://doi.org/10.1002/aenm.201703432
2. X. Zhu, D. Yang, R. Yang, B. Yang, Z. Yang et al., Superior stability for perovskite solar cells with 20% efficiency using

vacuum co-evaporation. Nanoscale **9**, 12316–12323 (2017). https://doi.org/10.1039/C7NR04501H

3. J. Huang, Y. Yuan, Y. Shao, Y. Yan, Understanding the physical properties of hybrid perovskites for photovoltaic applications. Nat. Rev. Mater. **2**, 17042 (2017). https://doi.org/10.1038/natrevmats.2017.42

4. P. Zhao, M. Yue, C. Lei, Z. Lin, J. Su et al., Device simulation of organic–inorganic halide perovskite/crystalline silicon four-terminal tandem solar cell with various antireflection materials. IEEE J. Photovolt. **8**, 1685–1691 (2018). https://doi.org/10.1109/JPHOTOV.2018.2869743

5. M. Jaysankar, M. Filipič, B. Zielinski, R. Schmager, W. Song et al., Perovskite–silicon tandem solar modules with optimised light harvesting. Energy Environ. Sci. **11**, 1489–1498 (2018). https://doi.org/10.1039/C8EE00237A

6. C.-H. Lin, B. Cheng, T.-Y. Li, J.R.D. Retamal et al., Orthogonal lithography for halide perovskite optoelectronic nanodevices. ACS Nano **13**(2), 1168–1176 (2018). https://doi.org/10.1021/ph4001108

7. C.C. Vidyasagar, B.M. Muñoz Flores, V.M. Jiménez Pérez, Recent advances in synthesis and properties of hybrid halide perovskites for photovoltaics. Nano-Micro Lett. **10**, 68 (2018). https://doi.org/10.1007/s40820-018-0221-5

8. NREL, Best Research-Cell Efficiency Chart, Photovoltaic Research, NREL. Natl. Renew. Energy Lab. (2019). https://www.nrel.gov/pv/cellefficiency.html

9. B. Conings, J. Drijkoningen, N. Gauquelin, A. Babayigit, J. D'Haen et al., Intrinsic thermal instability of methylammonium lead trihalide perovskite. Adv. Energy Mater. **5**, 1500477 (2015). https://doi.org/10.1002/aenm.201500477

10. Z. Song, A. Abate, S.C. Watthage, G.K. Liyanage, A.B. Phillips, U. Steiner, M. Graetzel, M.J. Heben, Perovskite solar cell stability in humid air: partially reversible phase transitions in the $PbI_2–CH_3NH_3I–H_2O$ system. Adv. Energy Mater. **6**, 1600846 (2016). https://doi.org/10.1002/aenm.201600846

11. Z. Zhang, J. Su, J. Hou, Z. Lin, Z. Hu et al., Potential applications of halide double perovskite Cs_2AgInX_6 (X = Cl, Br) in flexible optoelectronics: unusual effects of uniaxial strains. J. Phys. Chem. Lett. **10**, 1120–1125 (2019). https://doi.org/10.1021/acs.jpclett.9b00134

12. J. Zhang, J. Su, Z. Lin, M. Liu, J. Chang, Y. Hao, Disappeared deep charge-states transition levels in the p-type intrinsic $CsSnCl_3$ perovskite. Appl. Phys. Lett. **114**, 181902 (2019). https://doi.org/10.1063/1.5090420

13. L. Zhou, X. Guo, Z. Lin, J. Ma, J. Su et al., Interface engineering of low temperature processed all-inorganic $CsPbI_2Br$ perovskite solar cells toward PCE exceeding 14%. Nano Energy **60**, 583–590 (2019). https://doi.org/10.1016/j.nanoen.2019.03.081

14. A.E. Maughan, A.M. Ganose, D.O. Scanlon, J.R. Neilson, Perspectives and design principles of vacancy-ordered double perovskite halide semiconductors. Chem. Mater. **31**, 1184–1195 (2019). https://doi.org/10.1021/acs.chemmater.8b05036

15. F. Igbari, Z. Wang, L. Liao, Progress of lead-free halide double perovskites. Adv. Energy Mater. **9**, 1803150 (2019). https://doi.org/10.1002/aenm.201803150

16. T. Zhang, M.I. Dar, G. Li, F. Xu, N. Guo, M. Grätzel, Y. Zhao, Bication lead iodide 2D perovskite component to stabilize inorganic α-$CsPbI_3$ perovskite phase for high-efficiency solar cells. Sci. Adv. **3**, e1700841 (2017). https://doi.org/10.1126/sciadv.1700841

17. L.A. Frolova, D.V. Anokhin, A.A. Piryazev, S.Y. Luchkin, N.N. Dremova, K.J. Stevenson, P.A. Troshin, Highly efficient all-inorganic planar heterojunction perovskite solar cells produced by thermal coevaporation of CsI and PbI_2. J. Phys. Chem. Lett. **8**, 67–72 (2017). https://doi.org/10.1021/acs.jpclett.6b02594

18. M. Kulbak, D. Cahen, G. Hodes, How important is the organic part of lead halide perovskite photovoltaic cells? Efficient $CsPbBr_3$ cells. J. Phys. Chem. Lett. **6**, 2452–2456 (2015). https://doi.org/10.1021/acs.jpclett.5b00968

19. Q. Ma, S. Huang, X. Wen, M.A. Green, A.W.Y. Ho-Baillie, Hole transport layer free inorganic $CsPbIBr_2$ perovskite solar cell by dual source thermal evaporation. Adv. Energy Mater. **6**, 1502202 (2016). https://doi.org/10.1002/aenm.201502202

20. S. Xiang, Z. Fu, W. Li, Y. Wei, J. Liu et al., Highly air-stable carbon-based α-$CsPbI_3$ perovskite solar cells with a broadened optical spectrum. ACS Energy Lett. **3**, 1824–1831 (2018). https://doi.org/10.1021/acsenergylett.8b00820

21. Y. Zhang, S. Li, W. Yang, M.K. Joshi, X. Fang, Millimeter-sized single-crystal $CsPbrB_3$/CuI heterojunction for high-performance self-powered photodetector. J. Phys. Chem. Lett. **10**, 2400–2407 (2019). https://doi.org/10.1021/acs.jpclett.9b00960

22. Y. Zhang, W. Xu, X. Xu, J. Cai, W. Yang, X. Fang, Self-powered dual-color UV–green photodetectors based on SnO_2 millimeter wire and microwires/$CsPbBr_3$ particle heterojunctions. J. Phys. Chem. Lett. **10**, 836–841 (2019). https://doi.org/10.1021/acs.jpclett.9b00154

23. W. Ahmad, J. Khan, G. Niu, J. Tang, Inorganic CsPbI3 perovskite-based solar cells: a choice for a tandem device. Sol. RRL **1**, 1700048 (2017). https://doi.org/10.1002/solr.201700048

24. G. Murtaza, I. Ahmad, First principle study of the structural and optoelectronic properties of cubic perovskites $CsPbM_3$ (M = Cl, Br, I). Phys. B: Condens. Matter **406**, 3222–3229 (2011). https://doi.org/10.1016/j.physb.2011.05.028

25. M.I. Hossain, W. Qarony, S. Ma, L. Zeng, D. Knipp, Y.H. Tsang, Perovskite/silicon tandem solar cells: from detailed balance limit calculations to photon management. Nano-Micro Lett. **11**, 58 (2019). https://doi.org/10.1007/s40820-019-0287-8

26. H. Fu, V. Ramalingam, H. Kim, C. Lin, X. Fang, H.N. Alshareef, J. He, MXene-contacted silicon solar cells with 11.5% efficiency. Adv. Energy Mater. **9**, 190 (2019). https://doi.org/10.1002/aenm.201900180

27. X. Chang, W. Li, L. Zhu, H. Liu, H. Geng, S. Xiang, J. Liu, H. Chen, Carbon-based $CsPbBr_3$ perovskite solar cells: all-ambient processes and high thermal stability. ACS Appl. Mater. Interfaces **8**, 33649–33655 (2016). https://doi.org/10.1021/acsami.6b11393

28. Y. Wang, T. Zhang, M. Kan, Y. Zhao, Bifunctional stabilization of all-inorganic α-$CsPbI_3$ perovskite for 17% efficiency

photovoltaics. J. Am. Chem. Soc. **140**, 12345–12348 (2018). https://doi.org/10.1021/jacs.8b07927

29. X. Guo, B. Zhang, Z. Lin, J. Ma, J. Su et al., Interface engineering of TiO2/perovskite interface via fullerene derivatives for high performance planar perovskite solar cells. Org. Electron. **62**, 459–467 (2018). https://doi.org/10.1016/j.orgel.2018.08.039

30. P. Zhang, J. Wu, T. Zhang, Y. Wang, D. Liu et al., Perovskite solar cells with ZnO electron-transporting materials. Adv. Mater. **30**, 1703737 (2018). https://doi.org/10.1002/adma.201703737

31. P. Zhao, Z. Liu, Z. Lin, D. Chen, J. Su et al., Device simulation of inverted CH3NH3PbI3–xClx perovskite solar cells based on PCBM electron transport layer and NiO hole transport layer. Sol. Energy **169**, 11–18 (2018). https://doi.org/10.1016/j.solener.2018.04.027

32. W. Ouyang, F. Teng, J.-H. He, X. Fang, Enhancing the photoelectric performance of photodetectors based on metal oxide semiconductors by charge-carrier engineering. Adv. Funct. Mater. **29**, 1807672 (2019). https://doi.org/10.1002/adfm.201807672

33. M. Dehghan, A. Behjat, Deposition of zinc oxide as an electron transport layer in planar perovskite solar cells by spray and SILAR methods comparable with spin coating. RSC Adv. **9**, 20917–20924 (2019). https://doi.org/10.1039/C9RA01839E

34. S. Zhuang, X. Ma, D. Hu, X. Dong, B. Zhang, Air-stable all inorganic green perovskite light emitting diodes based on ZnO/CsPbBr3/NiO heterojunction structure. Ceram. Int. **44**, 4685–4688 (2018). https://doi.org/10.1016/j.ceramint.2017.12.048

35. J. Ma, Z. Lin, X. Guo, L. Zhou, J. Su et al., Low-temperature solution-processed ZnO electron transport layer for highly efficient and stable planar perovskite solar cells with efficiency over 20%. Sol. RRL **3**, 1900096 (2019). https://doi.org/10.1002/solr.201900096

36. P. Zhang, F. Yang, G. Kapil, Q. Shen, T. Toyoda et al., Enhanced performance of ZnO based perovskite solar cells by Nb2O5 surface passivation. Org. Electron. **62**, 615–620 (2018). https://doi.org/10.1016/j.orgel.2018.06.038

37. D. Zhang, X. Zhang, S. Bai, C. Liu, Z. Li, W. Guo, F. Gao, Surface chlorination of ZnO for perovskite solar cells with enhanced efficiency and stability. Sol. RRL (2019). https://doi.org/10.1002/solr.201900154

38. C. Liu, W. Li, C. Zhang, Y. Ma, J. Fan, Y. Mai, All-inorganic CsPbI2Br perovskite solar cells with high efficiency exceeding 13%. J. Am. Chem. Soc. **140**, 3825–3828 (2018). https://doi.org/10.1021/jacs.7b13229

39. L. Yan, Q. Xue, M. Liu, Z. Zhu, J. Tian et al., Interface engineering for all-inorganic CsPbI2Br perovskite solar cells with efficiency over 14%. Adv. Mater. **30**, 1802509 (2018). https://doi.org/10.1002/adma.201802509

40. L. Zhu, C. Chen, Y. Weng, F. Li, Q. Lou, Enhancing the performance of inverted perovskite solar cells by inserting a ZnO:TIPD film between PCBM layer and Ag electrode.

Sol. Energy Mater. Sol. Cells **198**, 11–18 (2019). https://doi.org/10.1016/j.solmat.2019.04.007

41. B. Jeong, H. Han, Y.J. Choi, S.H. Cho, E.H. Kim et al., All-inorganic CsPbI3 perovskite phase-stabilized by poly(ethylene oxide) for red-light-emitting diodes. Adv. Funct. Mater. **28**, 1706401 (2018). https://doi.org/10.1002/adfm.201706401

42. Q. Dong, C.H.Y. Ho, H. Yu, A. Salehi, F. So, Defect passivation by fullerene derivative in perovskite solar cells with aluminum-doped zinc oxide as electron transporting layer. Chem. Mater. **31**(17), 6833–6840 (2019). https://doi.org/10.1021/acs.chemmater.9b01292

43. J. Song, E. Zheng, L. Liu, X. Wang, G. Chen, W. Tian, T. Miyasaka, Magnesium-doped zinc oxide as electron selective contact layers for efficient perovskite solar cells. ChemSusChem **9**, 2640–2647 (2016). https://doi.org/10.1002/cssc.201600860

44. M.A. Mahmud, N.K. Elumalai, M.B. Upama, D. Wang, A.M. Soufiani, M. Wright, C. Xu, F. Haque, A. Uddin, Solution-processed lithium-doped ZnO electron transport layer for efficient triple cation (Rb, MA, FA) perovskite solar cells. ACS Appl. Mater. Interfaces **9**, 33841–33854 (2017). https://doi.org/10.1021/acsami.7b09153

45. M.M. Shabat, H.J. El-Khozondar, A.A. AlShembari, R.J. El-Khozondar, Transfer matrix method application on semiconductor-based solar cell characteristics measurements. Mod. Phys. Lett. B **32**, 1850346 (2018). https://doi.org/10.1142/S0217984918503463

46. S. Sajid, A.M. Elseman, J. Ji, S. Dou, D. Wei et al., Computational study of ternary devices: stable, low-cost, and efficient planar perovskite solar cells. Nano-Micro Lett. **10**, 51 (2018). https://doi.org/10.1007/s40820-018-0205-5

47. P. Zhao, L. Feng, Z. Lin, J. Wang, J. Su et al., Theoretical analysis of two-terminal and four-terminal perovskite/copper indium gallium selenide tandem solar cells. Sol. RRL (2019). https://doi.org/10.1002/solr.201900303

48. K. Cnops, B.P. Rand, D. Cheyns, B. Verreet, M.A. Empl, P. Heremans, 8.4% efficient fullerene-free organic solar cells exploiting long-range exciton energy transfer. Nat. Commun. **5**, 3406 (2014). https://doi.org/10.1038/ncomms4406

49. J.P. Perdew, K. Burke, M. Ernzerhof, Generalized gradient approximation made simple. Phys. Rev. Lett. **77**, 3865 (1996). https://doi.org/10.1103/PhysRevLett.77.3865

50. G. Kresse, D. Joubert, From ultrasoft pseudopotentials to the projector augmented-wave method. Phys. Rev. B **59**, 1758 (1999). https://doi.org/10.1103/PhysRevB.59.1758

51. G. Kresse, J. Furthmüller, Efficient iterative schemes for ab initio total-energy calculations using a plane-wave basis set. Phys. Rev. B **54**, 11169 (1996). https://doi.org/10.1103/PhysRevB.54.11169

52. X. Wei, X. Wang, H. Jiang, Y. Huang, A. Han, Q. Gao, J. Bian, Z. Liu, Numerical simulation and experimental validation of inverted planar perovskite solar cells based on NiOx hole transport layer. Superlattices Microstruct. **112**, 383–393 (2017). https://doi.org/10.1016/j.spmi.2017.09.048

53. E.M. Hutter, T.J. Savenije, Thermally activated second-order recombination hints toward indirect recombination in fully

inorganic CsPbI₃ perovskites. ACS Energy Lett. **3**, 2068–2069 (2018). https://doi.org/10.1021/acsenergylett.8b01106

54. B. Li, Y. Zhang, L. Fu, T. Yu, S. Zhou, L. Zhang, L. Yin, Surface passivation engineering strategy to fully-inorganic cubic CsPbI₃ perovskites for high-performance solar cells. Nat. Commun. **9**, 1076 (2018). https://doi.org/10.1038/s41467-018-03169-0

55. A.-A. Kanoun, M.B. Kanoun, A.E. Merad, S. Goumri-Said, Toward development of high-performance perovskite solar cells based on CH₃NH₃GeI₃ using computational approach. Sol. Energy **182**, 237–244 (2019). https://doi.org/10.1016/j.solener.2019.02.041

56. K. Mahmood, A. Khalid, M.T. Mehran, Nanostructured ZnO electron transporting materials for hysteresis-free perovskite solar cells. Sol. Energy **173**, 496–503 (2018). https://doi.org/10.1016/j.solener.2018.08.004

57. D.A. Neamen, Nanoscale transistors. Mater. Today **9**, 57 (2006). https://doi.org/10.1016/S1369-7021(06)71449-3

58. J. Ma, J. Chang, Z. Lin, X. Guo, L. Zhou et al., Elucidating the roles of TiCl₄ and PCBM fullerene treatment on TiO₂ electron transporting layer for highly efficient planar perovskite solar cells. J. Phys. Chem. C **122**, 1044–1053 (2018). https://doi.org/10.1021/acs.jpcc.7b09537

59. H.-J. Feng, J. Huang, X.C. Zeng, Photovoltaic diode effect induced by positive bias poling of organic layer-mediated interface in perovskite heterostructure α-HC(NH₂)₂PbI₃/TiO₂. Adv. Mater. Interfaces **3**, 1600267 (2016). https://doi.org/10.1002/admi.201600267

60. H. Choi, J. Jeong, H.-B. Kim, S. Kim, B. Walker, G.-H. Kim, J.Y. Kim, Cesium-doped methylammonium lead iodide perovskite light absorber for hybrid solar cells. Nano Energy **7**, 80–85 (2014). https://doi.org/10.1016/j.nanoen.2014.04.017

61. P. Luo, W. Xia, S. Zhou, L. Sun, J. Cheng, C. Xu, Y. Lu et al., Solvent engineering for ambient-air-processed, phase-stable CsPbI₃ in perovskite solar cells. J. Phys. Chem. Lett. **7**, 3603–3608 (2016). https://doi.org/10.1021/acs.jpclett.6b01576

62. A. Swarnkar, A.R. Marshall, E.M. Sanehira, B.D. Chernomordik, D.T. Moore, J.A. Christians, T. Chakrabarti, J.M. Luther, Quantum dot–induced phase stabilization of α-CsPbI₃ perovskite for high-efficiency photovoltaics. Science **354**, 92–95 (2016). https://doi.org/10.1126/science.aag2700

63. Q. Wang, X. Zheng, Y. Deng, J. Zhao, Z. Chen, J. Huang, Stabilizing the α-phase of CsPbI₃ perovskite by sulfobetaine zwitterions in one-step spin-coating films. Joule **1**, 371–382 (2017). https://doi.org/10.1016/j.joule.2017.07.017

64. C.F.J. Lau, Z. Wang, N. Sakai, J. Zheng, C.H. Liao et al., Fabrication of efficient and stable CsPbI₃ perovskite solar cells through cation exchange process. Adv. Energy Mater. **1901685**, 1901685 (2019). https://doi.org/10.1002/aenm.201901685

65. Y. Wang, M.I. Dar, L.K. Ono, T. Zhang, M. Kan et al., Thermodynamically stabilized β-CsPbI₃–based perovskite solar cells with efficiencies > 18%. Science **365**, 591–595 (2019). https://doi.org/10.1126/science.aav8680